nature communications

Article

https://doi.org/10.1038/s41467-025-64112-8

Inter-basin contrast in the Southern Ocean warming

Received: 13 December 2024

Accepted: 8 September 2025

Published online: 13 October 2025

Check for updates

Yuanyuan Song[1,2], Yuanlong Li[1,3] ✉, Gaël Forget[2], Aixue Hu[4], Qian Li[2,5], Jia-Rui Shi[6,7], Xiaodan Chen[8], Kai Ge[1] & Fan Wang[1,3]

The Southern Ocean (SO) is a major contributor to global ocean heat uptake, exhibiting deep-reaching warming trends within the 35°S-55°S band. Here, we reveal a notable inter-basin contrast in the SO warming rates. Over the past six decades, the warming of the 0-700 m Atlantic-Indian sector was 40.0 ± 5.7% faster than the Pacific sector, nearly doubling at ~44°S. Ocean-only and coupled model experiments suggest that this basin-scale contrast arises from alterations in wind-driven heat redistribution rather than surface heating. Specifically, the intensification and poleward migration of westerly winds are more prominent in the Atlantic-Indian sector, leading to stronger upper-layer heat convergence. The inter-basin warming contrast is projected to persist and amplify throughout the remainder of the 21st century. This study highlights the inter-basin contrast in the past and future SO warming, with useful implications for understanding regional changes in the SO climate, ice mass, and marine ecosystems.

The Southern Ocean (SO) has witnessed substantial warming trends since the mid-twentieth century[1–6], accounting for ~60% of the global ocean heat storage in the upper 2000 m layer[7,8]. Notably, the rate of SO warming has also accelerated, reaching 2.72 ± 0.29 ZJ yr^{-1} during 1991–2019—nearly double the rate of 1.49 ± 0.23 ZJ yr^{-1} during 1958–1990[9]. The SO warming has significant ramifications on sea ice[10] and ice shelves[11], the formation of abyssal waters[12–14], marine ecosystems and biodiversity around the Antarctic[15] and far-reaching impacts on climates over the globe[16,17].

The SO warming characterizes a prominent meridional structure with enhanced, deep-reaching warming trends extending to 2000 m between 35°S-55°S and a warming maximum on the northern flank of the Antarctic Circumpolar Current (ACC); by contrast, the surface layer of regions south of the ACC has not warmed significantly[2,5,18–20]. The "added heat" mechanism—involving heat uptake through surface heat fluxes and heat transport by the mean circulation—has been used to explain the meridional structure of SO warming[2,18,21]. The "anthropogenic heat" enters the ocean in regions south of the ACC and flows northward through Ekman currents under westerly winds[3,19,20,22]. The transport of warmed water across the ACC leads to heat convergence within the 35°S-55°S band[19,23] and subduction into the subsurface ocean with mode and intermediate waters[24–26]. The "redistributed heat" mechanism dominated by changes in ocean circulation was believed to play a secondary role in shaping this meridional structure[2,19,27]. Meanwhile, mesoscale and sub-mesoscale processes within the ACC partly offset the wind-driven northward heat transport[28,29]. Experiments based on an ocean model suggested that both winds and heat flues contribute to the enhanced heat uptake by the SO[30].

Compared to the well-documented meridional structure, the zonal structure of SO warming has been less appreciated. Zonally asymmetric features were often overlooked owing to the common practice of circumpolar[3,19] or regional[30] mean diagnostics. A recent study based on ocean model simulations revealed complex asymmetric features in the

[1]Key Laboratory of Ocean Observation and Forecasting and Laboratory of Ocean Circulation and Waves, Institute of Oceanology, Chinese Academy of Sciences, Qingdao, China. [2]Department of Earth, Atmospheric and Planetary Sciences, Massachusetts Institute of Technology, Cambridge, MA, USA. [3]Laboratory for Ocean Dynamics and Climate, Qingdao Marine Science and Technology Center, Qingdao, China. [4]Climate and Global Dynamics Laboratory, National Center for Atmospheric Research, Boulder, CO, USA. [5]Department of Earth, Ocean, and Atmospheric Science, Florida State University, Tallahassee, FL, USA. [6]Woods Hole Oceanographic Institution, Woods Hole, MA, USA. [7]Courant Institute of Mathematical Sciences, New York University, New York, USA. [8]Department of Atmospheric and Oceanic Sciences, Institute of Atmospheric Sciences, Fudan University, Shanghai, China. ✉e-mail: liyuanlong@qdio.ac.cn

https://doi.org/10.1038/s41467-025-64112-8

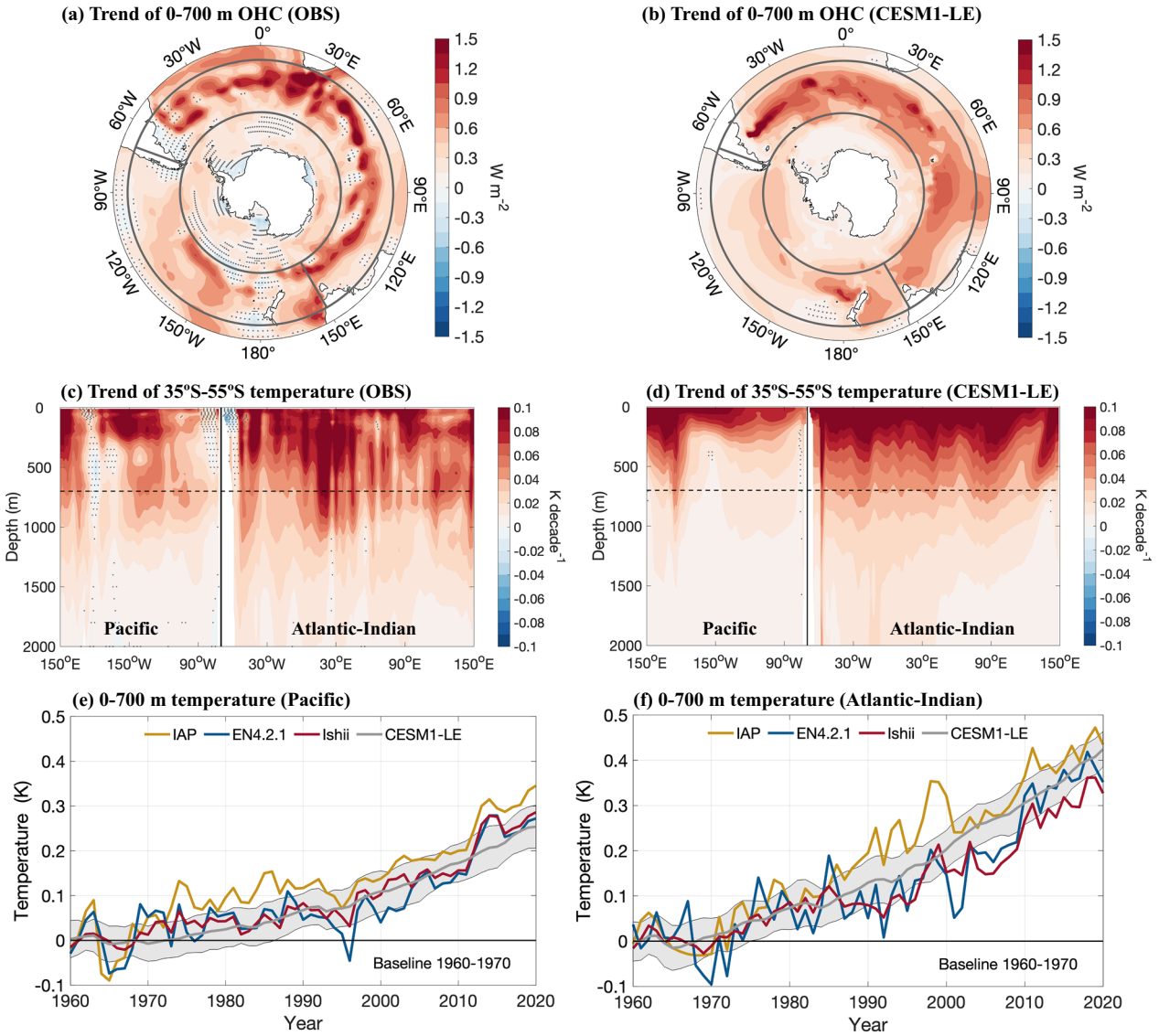

Fig. 1 | Temperature change in the Southern Ocean. a, **b** Linear trends of 0-700 m ocean heat content (OHC) for the period of 1960-2020 derived from the average of the Institute of Atmospheric Physics (IAP) ocean analysis data[7,63], the version 4.2.2 of the Met Office Hadley Centre "EN" series of datasets (EN4)[35], and the 2017 version of Ishii analysis data[34]; see "Methods") and CESM1-LE ensemble-mean. Grey curves indicate the zonal belt of 35°S-55°S where the Pacific and Atlantic-Indian sectors are separated by 70°W and 150°E. **c**, **d** Meridional mean (35°S-55°S) temperature trends for the same period in observations and CESM1-LE ensemble mean. The horizontal dashed line denotes the depth of 700 m and the vertical black line indicates 70°W. Stippling indicates insignificant changes at the 95% confidence level. **e**, **f** Time series of averaged 0–700 m temperature in the Pacific and Atlantic-Indian sectors, based on observations and CESM1-LE. All variables are shown as anomalies relative to the 1960–1970 baseline. Grey shading shows the one standard deviation range of CESM1-LE members. The CESM1-LE results analyzed here consist of the historical simulation of 1960–2005 and Representative Concentration Pathway (RCP) 8.5 projection of 2006–2100.

SO warming pattern of 1979–2019 and complex forcing effects of surface winds, heat flux, and freshwater flux, with the dominant driver varying with latitude[31]. Yet, the results of Ref. 31. for the four-decade period contain both the externally forced long-term changes and internal variability. Particularly, pronounced decadal variability arising from Interdecadal Pacific Oscillation can cause out-of-phase heat content changes between the Pacific and Atlantic–Indian sectors of the SO[32]; observation-based analysis suggested that wind forcing dominated the decadal warming of the Subantarctic Mode Water during 2005–2015[25]. Therefore, whether these recently revealed asymmetric warming patterns and the underlying mechanisms[30–32] are robust features of the SO under anthropogenic greenhouse warming remain uncertain.

Here, based upon established understanding[30–32], this study pursues further insights into asymmetric patterns of the SO heat storage under anthropogenic warming and the drivers. We will attempt to reveal a key asymmetric feature of anthropogenic heat storage in the SO—the notable inter-basin contrast with significantly stronger warming rates in the Atlantic and Indian sectors than the Pacific sector—consistently standing out from updated observational datasets[7,33–35] since 1960 and climate model simulations under historical and 21st-century scenarios (Fig. 1). Diagnosis using large-ensemble simulations of Community Earth System Model version-1 (CESM1-LE)[36] and sensitivity experiments using a standard-alone ocean model[37] uniformly suggest that this pattern is primarily shaped by asymmetric changes in westerly winds under anthropogenic climate change, rather than surface heat fluxes. Specifically, strengthening and southward migration of westerly winds are systematically more prominent in the Atlantic-Indian sector, causing stronger upper-layer warming in the 35°S-55°S band of this sector through oceanic heat redistribution. These results highlight the central

role of redistributed heat in shaping the zonal structure of SO warming, despite the well-established meridional structure shaped by added heat.

Inter-basin warming contrast

We start by looking at the 0–700 m OHC trends during 1960–2020 based on three observational datasets[7,33–35] (Fig. 1a). Within the enhanced warming band of 35°S-55°S, we detect a zonal asymmetry with the Atlantic-Indian sector (defined east of 70°E and west of 150°E here) warming evidently faster than the Pacific sector (west of 70°E and east of 150°E). In the Atlantic-Indian sector, a warming maximum emerges at ~45°S along the northern flank of the ACC—a feature unseen in the Pacific sector. Strong warming trends extend down to ~1000 m in the Atlantic-Indian sector but are mostly confined within the upper 300 m in the Pacific (Fig. 1c). This inter-basin contrast is consistently seen across three observational datasets, despite differences in details (Supplementary Fig. 1). This contrast also exists in the intermediate layer of 700–2000 m but much weaker in warming magnitudes (Supplementary Fig. 2). Given more limited observation sampling in deeper layers, hereafter we focus on the warming features in the upper 700 m layers.

The ensemble-mean of CESM1-LE largely replicates the warming pattern, although the warming maximum in the Atlantic-Indian sector is weaker and shifted southward compared to observations (Fig. 1b). CESM1-LE also captures the inter-basin contrasts in both warming magnitude and vertical structure (Fig. 1d). Meanwhile, CESM1-LE overestimates the near-surface warming, likely associated with the common biases of stronger upper-ocean stratification and shallower mixed layer in coupled models[38,39]. The overall consensus between observations and CESM1-LE ensemble mean indicates that this inter-basin contrast in heat storage represents a robust feature of the SO under anthropogenic climate change. In fact, this contrast is discernible in most of the 40 members of CESM1-LE (not shown), reflecting the dominance of external forcing over internal variability in the SO heat storage pattern.

In the observations, the Pacific sector has an average warming rate of 0.05 ± 0.01 K decade^{-1} in the 0–700 m layer (Supplementary Fig. 3), corresponding to a 60-year warming of 0.30 ± 0.04 K by 2020 relative to the 1960–1970 baseline (Fig. 1e). By contrast, the Atlantic-Indian sector warms at a rate of 0.07 ± 0.01 K decade^{-1} (Supplementary Fig. 3), resulting in a 60-year warming of 0.42 ± 0.07 K (Fig. 1f). The warming of the Atlantic-Indian sector is $46.7 \pm 10.7\%$ stronger than that of the Pacific sector. The weaker contrast over 1990–2020 implies the influence of decadal variability on shorter-period change (Supplementary Fig. 3). However, this contrast existed in both the Argo (2004–2020) and pre-Argo (1960–2003) periods. Notably, the Argo era witnessed accelerated warming than before in both sectors, partly owing to enhanced observational sampling that can more sufficiently resolve the warming trends. At the heat storage maximum of ~44°S, the warming of Atlantic-Indian sector was nearly twice as strong as the Pacific sector (Supplementary Fig. 4a, b). The inter-basin contrast is generally insensitive to the choice of the ending year in trend calculation. Although fluctuated by decadal variability[32], the stronger warming of the Atlantic-Indian sector is a persistent feature throughout 1960–2020. In CESM1-LE simulations, the Pacific and Atlantic-Indian sectors warm at rates of 0.04 ± 0.01 and 0.07 ± 0.01 K decade^{-1}, respectively, indicating an inter-basin contrast of $68.4 \pm 39.0\%$—greater than the observed contrast of $40.0 \pm 5.7\%$. This difference reflects the weaker subsurface warming in the central Pacific and stronger surface warming in the Atlantic-Indian sector in CESM1-LE ensemble-mean. This can be partly explained by decadal internal variability[32] that causes warmer Pacific sector in observation than in CESM1-LE ensemble-mean since 2012 (Fig. 1e).

Surface heat uptake versus wind-driven heat redistribution

Surface heat flux-driven heat uptake and wind-driven ocean heat redistribution are two key mechanisms potentially shaping the SO heat storage pattern[2,20,30–32,40–43]. To explore their relative importance, we first look at trends of surface net heat flux Q_{net} and surface winds during 1960–2020 (Fig. 2). The trend of Q_{net} (Fig. 2a and Supplementary Fig. 5a) suggests prevailing surface heating in the high-latitude seas around Antarctica and heat release toward the atmosphere in the mid-latitudes north of 50°S (Supplementary Fig. 5c and Supplementary Fig. 6a). Interestingly, on average, the Pacific sector (1.08 W m^{-2} decade^{-1}) receives stronger surface heating than the Atlantic-Indian sector (0.42 W m^{-2} decade^{-1}) in the high-latitudes in ERA5. This feature is further supported by Japanese 55-year Reanalysis (JRA-55) data, with 0.57 W m^{-2} decade^{-1} in the Pacific sector versus 0.29 W m^{-2} decade^{-1} in the Atlantic-Indian sector. These results indicate surface heating cannot explain the asymmetric pattern of heat storage.

Westerlies over the SO have intensified during 1960–2020 (Fig. 2b), due to a combination of stratospheric ozone depletion, greenhouse gas forcing, and tropical natural variability[44–48]. The strengthened westerlies accompany trends of negative wind stress curls (WSCs) south of 55°S and positive WSCs north of this latitude, which enhances the northward ocean heat transport from high latitudes and heat convergence in the mid-latitudes[27]. Similar trend patterns are seen in the JRA-55 data (Supplementary Fig. 5). In addition to prevailing intensification across sectors, the inter-basin contrast with a stronger intensification in the Atlantic-Indian sector is significant at 90% confidence level. This contrast in surface winds caused stronger anomalous northward ocean heat transport and heat convergence north of 45°S in the Atlantic-Indian sector than in the Pacific—a candidate explanation for the inter-basin contrast in heat storage.

In CESM1-LE, there are prevailing trends of positive Q_{net} at all latitudes of the SO (Fig. 2c and Supplementary Fig. 6b), in contrast to the mid-latitude heat loss in ERA5 (Fig. 2a and Supplementary Fig. 6a). This discrepancy is linked to insufficient strengthening of westerly winds compared to observation-based changes and easterly trends in mid-latitude regions (Fig. 2d)—a common bias among IPCC-class climate models[39,49], which reduces the total wind speed and suppresses heat release there. The underestimated heat uptake in the high latitudes is likely due to overestimated surface warming and absence of regional cooling trends around the Antarctic in models[50]. Nevertheless, the surface heating in the Pacific sector is also stronger than in the Atlantic-Indian sector (0.24 versus 0.16 W m^{-2} decade^{-1}), unable to account for the SO warming asymmetry. CESM1-LE also produces asymmetric changes in westerly winds, although much weaker than changes in ERA5 and JRA-55.

To better visualize the inter-basin contrast, we compare meridional profiles of zonal-mean Q_{net} and WSC of the two sectors (Fig. 3). To account for influence of sea-ice cover, here we calculate area-weighted average Q_{net} only for open-ocean regions. Consistent with Fig. 2a, the Pacific sector receives stronger anomalous heat fluxes than the Atlantic-Indian sector in the high latitudes (south of 55°S) (Fig. 3a, b). The high-latitude Pacific sector loses heat to the atmosphere in the climatology, which weakened at ~1.0 W m^{-2} decade^{-1} since 1960; meanwhile, the heat uptake in the Atlantic-Indian counterpart increased at a rate of ~0.4 W m^{-2} decade^{-1} (Fig. 3b). In CESM1-LE, changes in Q_{net} can neither explain the inter-basin contrast in heat storage (Supplementary Fig. 6b and Supplementary Fig. 7a). The positive WSCs north of 55°S are enhanced in both sectors (Fig. 3c, d and Supplementary Fig. 5d). This enhancement is more pronounced in the Atlantic-Indian sector (0.61×10^{-8} Pa m^{-1} decade^{-1}) than in the Pacific sector (0.49×10^{-8} Pa m^{-1} decade^{-1}) in ERA5, which is also the case in JRA-55 (0.35×10^{-8} versus 0.28×10^{-8} Pa m^{-1} decade^{-1}). Notably, in the Atlantic-Indian sector, the trend indicates a poleward shift of the climatological WSC distribution[51–53]. Climate models tend to overestimate this trend[54,55], including CESM1-LE[56]. To summarize, these

https://doi.org/10.1038/s41467-025-64112-8

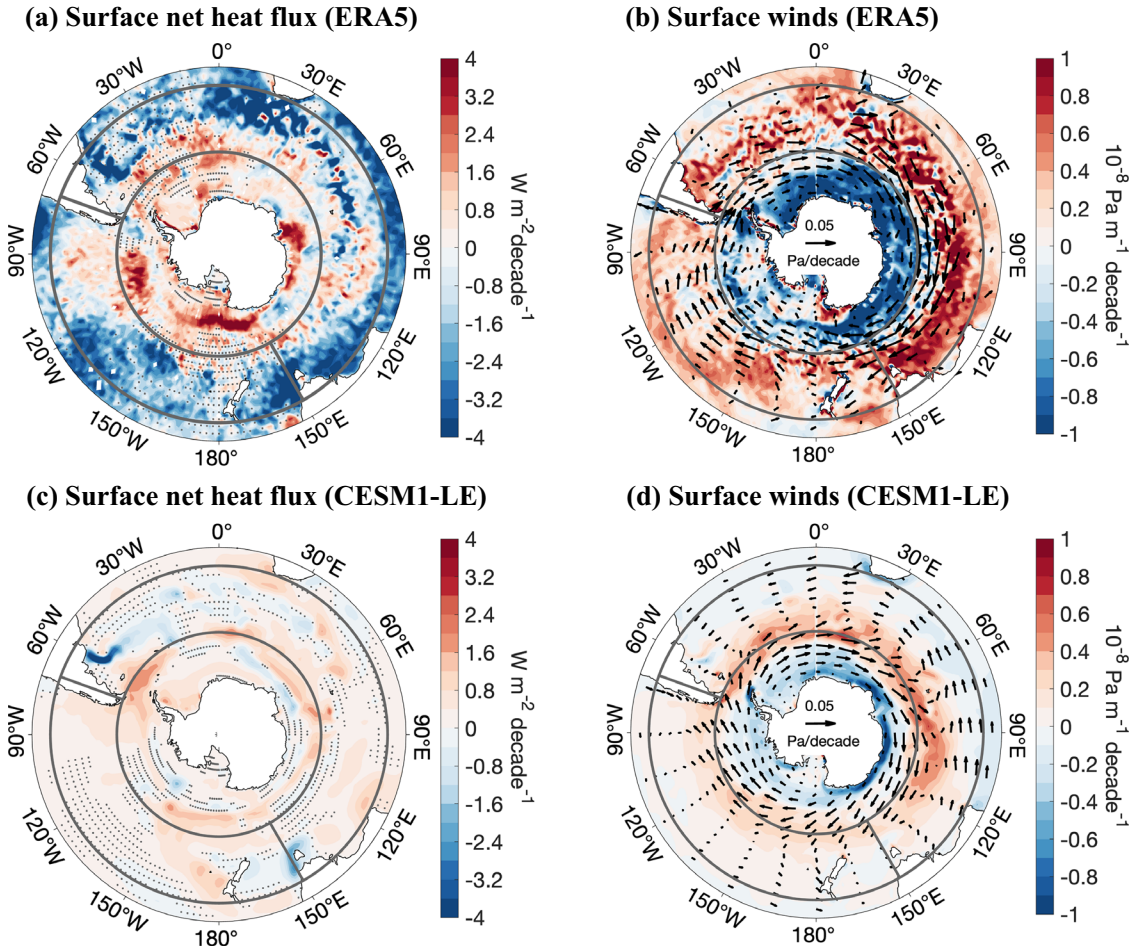

Fig. 2 | Changes in surface heating and winds over the Southern Ocean. **a**, **b** Linear trends in surface net heat flux (Q_{net}) and wind stress curl (WSC; shading) for the period of 1960–2020, based on European Centre for Medium-Range Weather Forecasts (ECMWF) reanalysis dataset version 5 (ERA5). In **b** trends of wind stress are show as vectors. **c**, **d** Linear trends in Q_{net} and WSC over 1960-2020 derived from CESM1-LE ensemble-mean. Stippling in (**a**–**d**) indicates insignificant changes at the 95% confidence level.

results suggest that wind changes, rather than Q_{net}, can explain the observed inter-basin warming contrast in the SO.

To understand how surface wind changes affect heat storage, we calculate ocean heat transports (Methods) (Fig. 4). In the SO, the meridional ocean heat transport (MOHT) driven by westerly winds is primarily facilitated by Ekman currents in the near-surface layer[19,20]. The 0–100 m MOHT, predominantly undertaken by Ekman currents, has strengthened in both sectors and dramatically shifted poleward in the Atlantic-Indian sector in CESM1-LE (Supplementary Fig. 7b). We further calculate the divergence of MOHT (Fig. 4a–d), i.e., ∂MOHT/∂y, which measures the heating effect exerted on the upper SO by MOHT. In the climatology, the MOHT shows divergence and convergence, indicated by positive and negative ∂MOHT/∂y values on the southern and northern flanks of the westerly maximum at ~47°S, respectively. They also correspond to climatologically positive and negative WSCs, respectively (Fig. 3c). Although the heat convergence (negative ∂MOHT/∂y) between 35°S-55°S is overall enhanced in both sectors, the convergent trends in the Atlantic-Indian sector are evidently stronger and cover a wider latitude range than those in the Pacific. Similar patterns are also seen in the heat convergence of Ekman currents, $\partial MOHT_E/\partial y$, as estimated using ERA5 winds (Fig. 4c, d). This feature is in line with the inter-basin contrast in surface wind changes (Fig. 2b, d) which shows stronger positive WSC trends and a larger poleward displacement of the WSC structure in the Atlantic-Indian sector (Fig. 3c, d).

Accompanied with heat convergence, there is prevailing downward heat flux (Methods) within the 35°–55°S band, penetrating to the subsurface ocean in both sectors (Fig. 4c, d). This downward heat flux is also evidently stronger in the Atlantic-Indian sector, particularly in the upper 1000 m layer. Trends of downward heat flux also penetrate deeper in the Atlantic-Indian sector than in the Pacific sector, consistent with the inter-basin contrast in the vertical structure of warming (Fig. 1d). Overall, these results highlight the essence of the time-varying wind-driven upper-ocean circulation in shaping the salient inter-basin contrast in the SO heat storage.

Zonal exchange between the two sectors may also contribute to the asymmetric warming features[25]. To examine this process, we further calculate the zonal ocean heat transport (ZOHT) integrated from 35°S to Antarctic coasts using CESM1-LE. The ZOHT from the Indian Ocean to the Pacific and that from the Pacific to the Atlantic are shown at 150°E, south of Australia, and at 70°W, within the Drake Passage, respectively (Supplementary Fig. 8). In CESM1-LE, the ZOHT has increased at both 150°E and 70°W, reflecting the acceleration of some regions in the north of the ACC[57] (although not through Drake Passage) and warming of the transported waters carried by the ACC. Since 1960, the heat transport from the Indian Ocean to the Pacific sector has increased by 1.1×10^{13} W decade^{-1}, slower than the heat transport increase of 1.7×10^{13} W decade^{-1} at Drake Passage, with the difference significant at the 90% confidence level. This suggests a net heat loss of the Pacific sector to the Atlantic-Indian sector through ZOHT. The increase in heat transport has not been confirmed by in-situ observations within the Drake Passage[5], possibly owing to insufficient sampling in spatial and temporal coverage of data. In addition,

https://doi.org/10.1038/s41467-025-64112-8

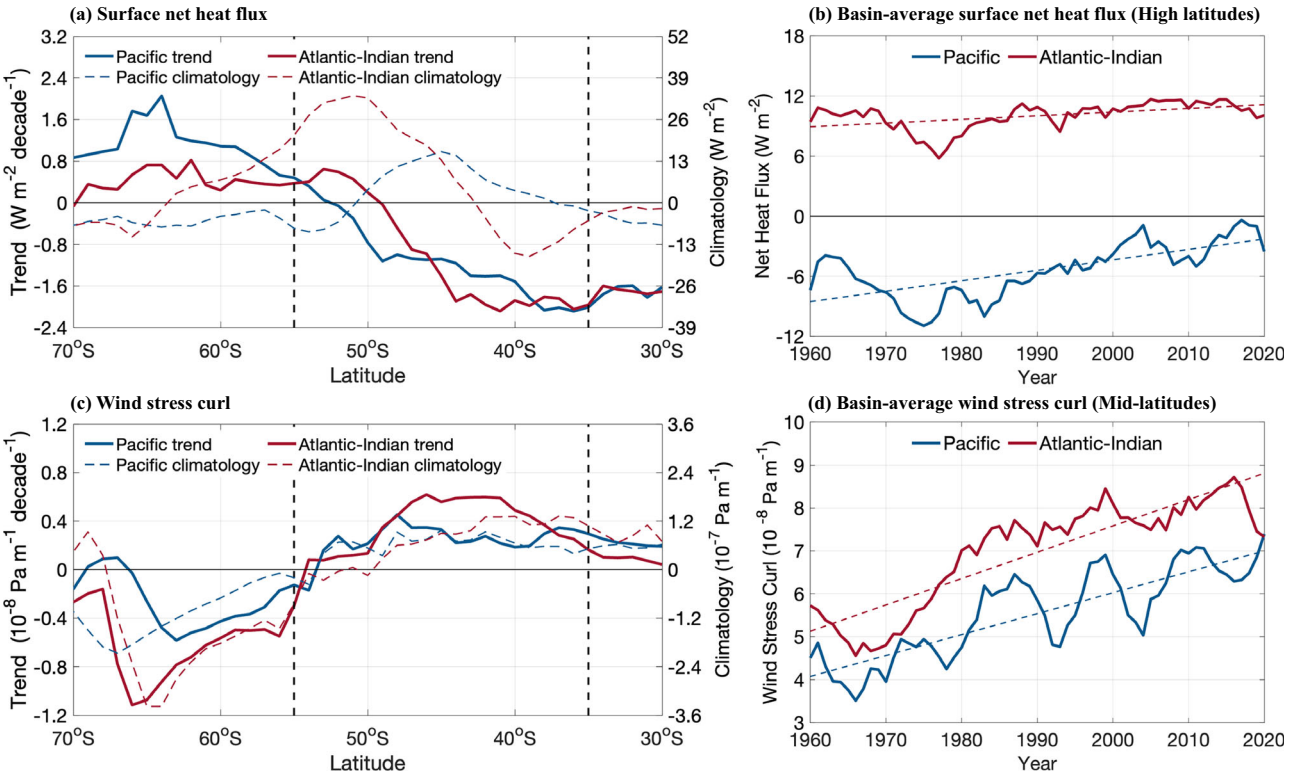

Fig. 3 | Inter-basin contrast in surface net heat flux (Q_{net}) and wind stress curl (WSC). a, **c** Linear trends (solid curves) and annual climatology (dashed curves) of zonal-mean Q_{net} and WSC in the Pacific (from 150°E to 70°W) and Atlantic-Indian (from 70°W to 150°E) sectors during 1960–2020. Black dashed lines denote 55°S and 35°S. **b**, **d** Average high-latitude (55°S-70°S) Q_{net} in open-ocean regions (annual mean sea ice concentration <50%) and average mid-latitude (35°S-55°S) WSC in the Pacific and Atlantic-Indian sectors based on ERA5 reanalysis. Dashed lines in (**b**, **d**) denote the linear regression.

changes in CESM1-LE represent externally forced trends that are still undetectable in the short observational records containing internal variability.

Insights from ocean model experiments

Analysis of observational data and CESM1-LE presented above overall points to the essence of wind-driven heat redistribution in shaping the zonal asymmetry of the SO heat storage pattern. To validate this conclusion and gain further insights, we employ stand-alone ocean models to perform simulations and experiments (Methods). The control simulation (CTRL) of the LASG/IAP Climate Ocean Model (LICOM) version-3[37] forced with daily surface atmospheric fields of ERA5[58] has well reproduced the observed heat storage pattern in the SO of 1960-2020, showing enhanced warming within the mid-latitude band of the Atlantic-Indian sector (Fig. 5a), albeit with stronger trends. Compared to the observed structure, the simulated warming band is shifted equatorward, and the heat storage near the western boundary of Pacific sector is overestimated. These discrepancies are likely associated with coarse model resolution (1°) which leads to underestimation of mesoscale eddies. The poleward heat transport induced by eddies act to compensate the wind-driven heat transport and the resultant heat convergence. Therefore, we adopt the central-to-eastern Pacific region of 180°-70°E, 35°S-50°S to quantify its weaker warming trend (0.06 K decade^{-1}) than that of the Atlantic-Indian sector (70°E-150°E, 35°S−-50°S; 0.09 K decade^{-1}) (Fig. 5b). A simulation with the Massachusetts Institute of Technology General Circulation Model (MITgcm)[59] forced by ERA5 fields also captures the inter-basin contrast in the SO warming (Supplementary Fig. 9). MITgcm provides an additional support of surface atmospheric changes in shaping the inter-basin contrast. The inter-basin contrast in LICOM and MITgcm is weaker than in observation and CESM1-LE, possibly owing to the lack of air-sea coupling in ocean-only models.

Then, we carried out two sensitivity experiments using LICOM to separate the effects of surface heating and wind forcing (Methods). The heat flux (HTFL) or wind-forcing (WND) simulations retain temporal changes only in surface heat fluxes or winds, respectively, while keeping other forcing fields invariant. The sum of HTFL and WND (Fig. 5c, d) closely resembles CTRL in warming pattern, indicating a negligible nonlinear effect between surface heating and wind-forcing and the robustness of our diagnoses. HTFL represents the storage of added heat[41] - with warming signatures generated by surface heating and transported by the climatological ocean circulation. This experiment produces quasi-uniform warming over the 35°S-50°S band (Fig. 5e, f). Note that the warming of the Atlantic-Indian sector is slightly weaker than the Pacific sector, 0.05 versus 0.06 K decade^{-1}, owing to inhomogeneous surface heating (Figs. 2 and 3). The results of HTFL confirm that surface heat fluxes cannot account for the observed inter-basin contrast, although heat fluxes can cause some symmetric features in heat storage[19,20].

WND largely represents the storage of redistributed heat[41] with warming signatures arising from heat redistribution induced by changes in wind-driven ocean circulations. This experiment produces enhanced heat pile-up in the 35°S-50°S band of the Atlantic-Indian Ocean sector (0.03 K decade^{-1}) without additional heat uptake (Fig. 5g, h), in contrast to insignificant trends in the central-to-eastern Pacific sector. The results of WND confirm that the inter-basin contrast in the SO heat storage results mainly from wind-driven upper-ocean heat redistribution. Note that the effect of mode water subduction[19,25] is also contained in WND, given that key factors determining the subduction rate, such as Ekman pumping and the mixed layer depth, are primarily controlled by winds. There are cooling trends in many regions in WND, which reflects a vertical redistribution of heat:

https://doi.org/10.1038/s41467-025-64112-8

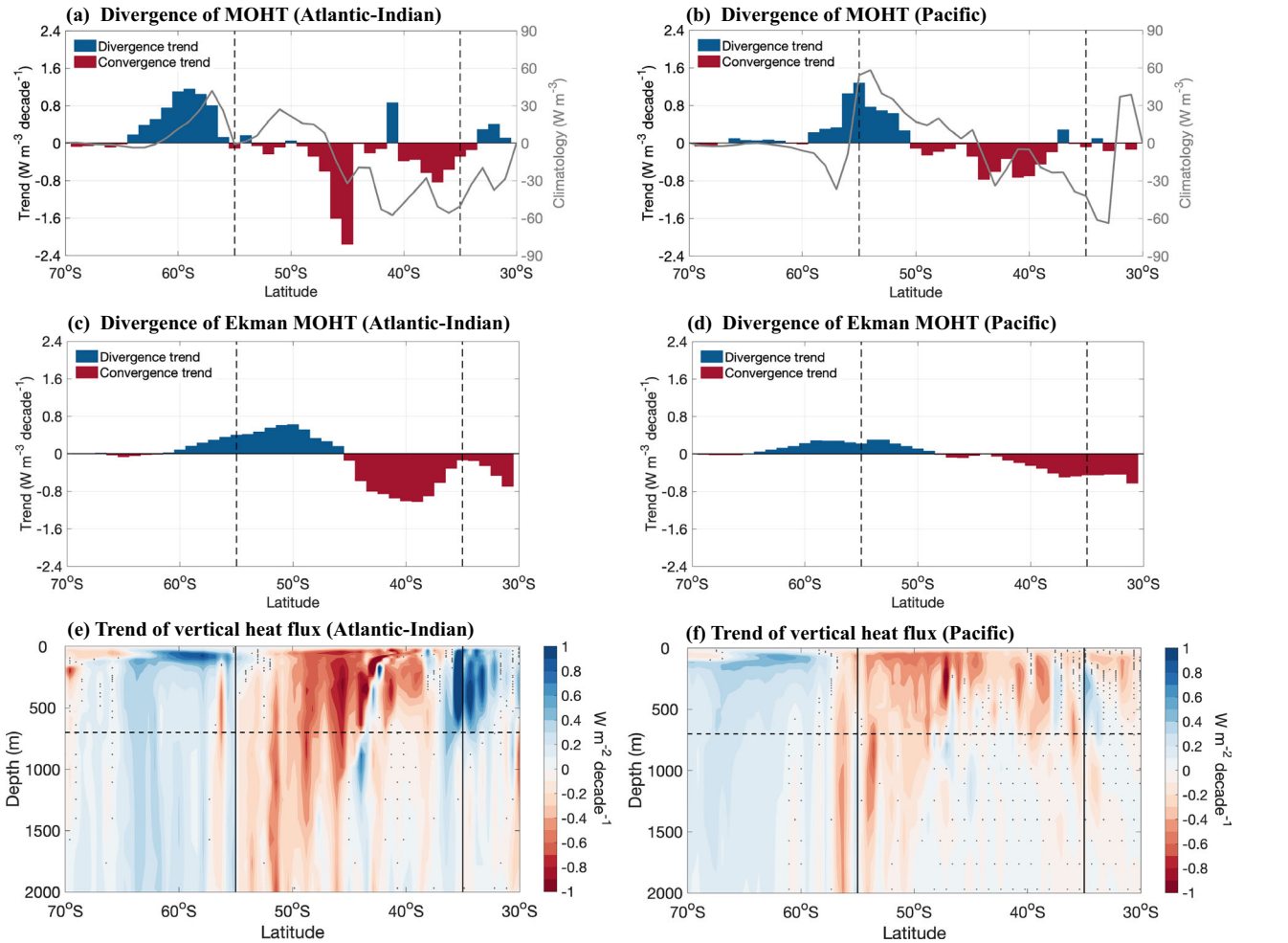

Fig. 4 | Inter-basin contrast in ocean heat transport. a, **b** Linear trends (red and blue bars) and climatology (grey curves) of divergence of 0–100 m meridional ocean heart transport (MOHT), $\partial MOHT/\partial y$, divided by the corresponding area in the Atlantic-Indian and Pacific sectors in CESM1-LE. **c**, **d** Linear trends of divergence of 0–100 m Ekman MOHT, $\partial MOHT_E/\partial y$, based on ERA5 data (see Methods). In **a**–**d** black dashed lines denote 55°S and 35°S. **e**, **f** Linear trend of zonal mean vertical heat flux ($\rho_0 c_p w\theta$) in the Atlantic-Indian and Pacific sectors in CESM1-LE simulation. The dashed line shows the depth of 700 m. Stippling indicates insignificant changes at the 95% confidence level.

enhanced northward transport under westerly winds brings cold waters from higher latitudes, while the downwelling moves upper-layer warm waters to the deep (Supplementary Fig. 10). LICOM experiments indicate that wind-driven heat redistribution also plays a role in shaping the meridional structure of warming, in addition to the zonal asymmetry (Supplementary Fig. 11). Specifically, while surface heating leads to prevailing warming in the 35°S-55°S band[3,19,20,22], the intensified westerly winds are essential for the warming maximum at ~40°S (at ~44°S in observation) in the Atlantic-Indian sector (Supplementary Fig. 11a).

Discussion and implications

Our work highlights the necessity of looking forward into the future changes in the SO based on projections of climate models. CESM1-LE project that the Atlantic-Indian sector will continue to warm faster than the Pacific sector in the 21st century under the high-emission RCP 8.5 scenario (Fig. 6a). Furthermore, in projections of Coupled Model Intercomparison Project phase 6 (CMIP6) models, the 0-700 m warming of the Atlantic-Indian sector will reach 1.01 ± 0.36°C, 1.63 ± 0.45°C, and 2.56 ± 0.76°C by 2100 relative to the 1960–1980 baseline under Shared Socioeconomic Pathway (SSP) 1-2.6, 2-4.5, and 5-8.5 scenarios, in contrast to the 0.72 ± 0.28°C, 1.10 ± 0.41°C, and 1.72 ± 0.65°C values of the Pacific sector. The inter-basin contrast of SO warming will further amplify throughout the 21st century under SSP5-8.5 and SSP2-4.5 scenarios (Fig. 6b). Under the low-emission scenario of SSP1-2.6, the contrast will diminish by the mid-21st century, showing close warming rates in the two sectors; the SO warming will terminate by the 2070s. The dependence on emission scenario highlights the essential role of greenhouse gases in generating the inter-basin warming contrast. Therefore, the inter-basin contrast is a robust feature of the SO under anthropogenic climate change and will probably persist or amplify in the upcoming decades.

To summarize, this study reveals the critical role of wind-driven heat redistribution in shaping the inter-basin warming contrast in the mid-latitude band (35°S-55°S) of the SO (Fig. 6a). This finding complements the existing view that emphasizes surface heat uptake and mean-circulation advection in the meridional structure of the SO warming. Based on recent studies that have reported asymmetric features of the SO warming[30–32], our work achieves the following distinct insights. First, we highlight the inter-basin contrast—with significantly stronger warming of the Atlantic-Indian sector than the Pacific sector—as a representative asymmetric feature within the enhanced warming band of 35°S-55°S. Second, inhomogeneous changes in the westerly winds, showing more prominent intensification and poleward migration in the Atlantic-Indian sector, play the dominant role in causing the inter-basin warming contrast through driving changes in ocean circulation and heat transport. Third, through combining climate model simulations, we show that the inter-basin

https://doi.org/10.1038/s41467-025-64112-8

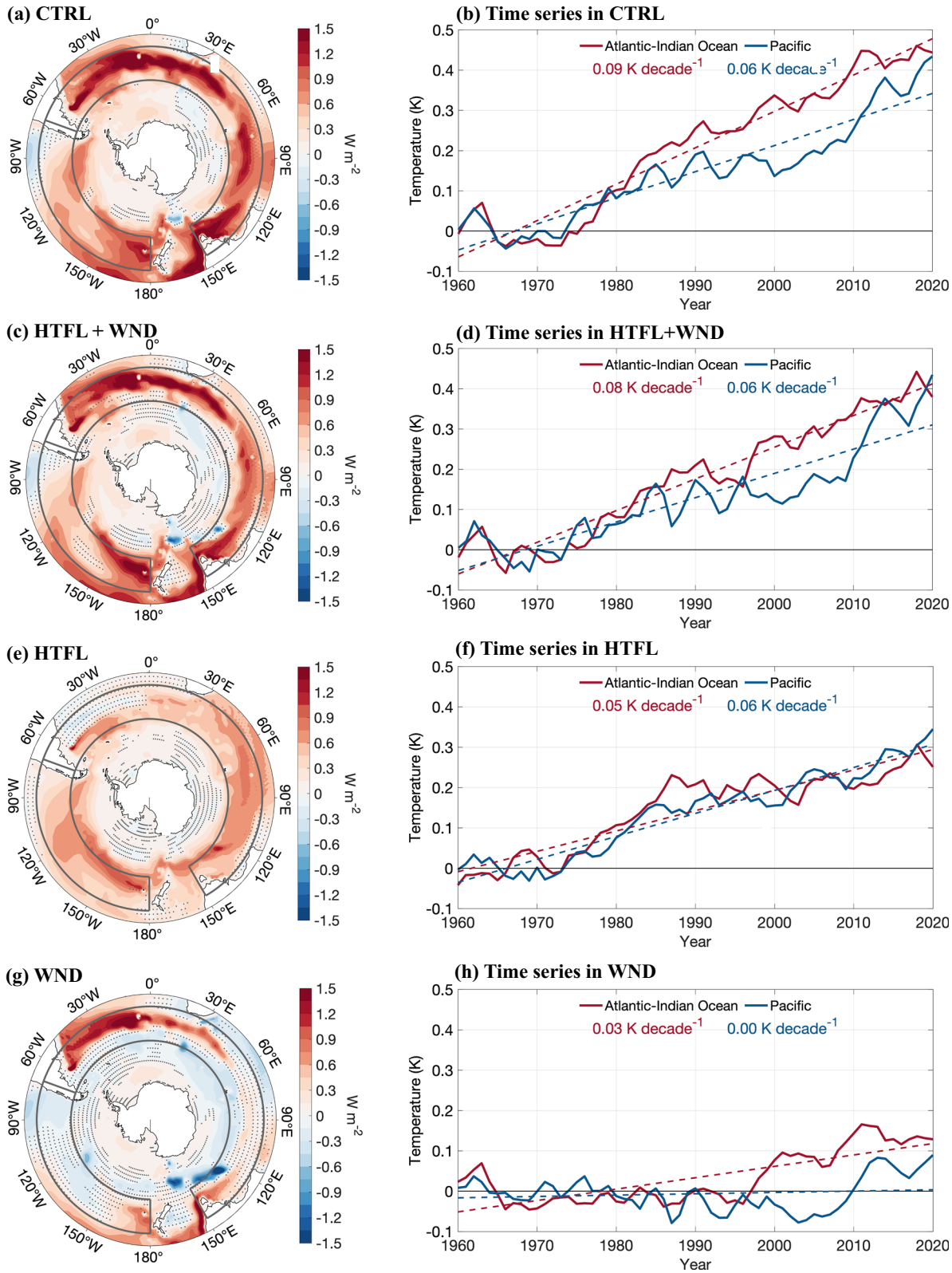

Fig. 5 | Heat storage and the inter-basin contrast in LICOM experiments. **a**, **c**, **e**, **g** Linear trends in 0–700 m ocean heat content (OHC) for the period of 1960-2020 in the control (CTRL, **a**), heat flux (HTFL, **c**), and wind (WND, **d**) experiments of LICOM and the sum HTFL and WND (**b**). Stippling indicates insignificant changes at the 95% confidence level. **b**, **d**, **f**, **h** The 0–700 m average temperatures for the central-to-eastern Pacific (180°-70°E, 35°S-50°S) and Atlantic-Indian (70°E-150°E, 35°S-50°S) sectors in the CTRL (**e**), HTFL (**g**), and WND (**h**) experiments of LICOM and the sum HTFL and WND (**f**). Dashed line in (**b**, **d**, **f**, **h**) indicates the least squares fit to corresponding time series.

https://doi.org/10.1038/s41467-025-64112-8

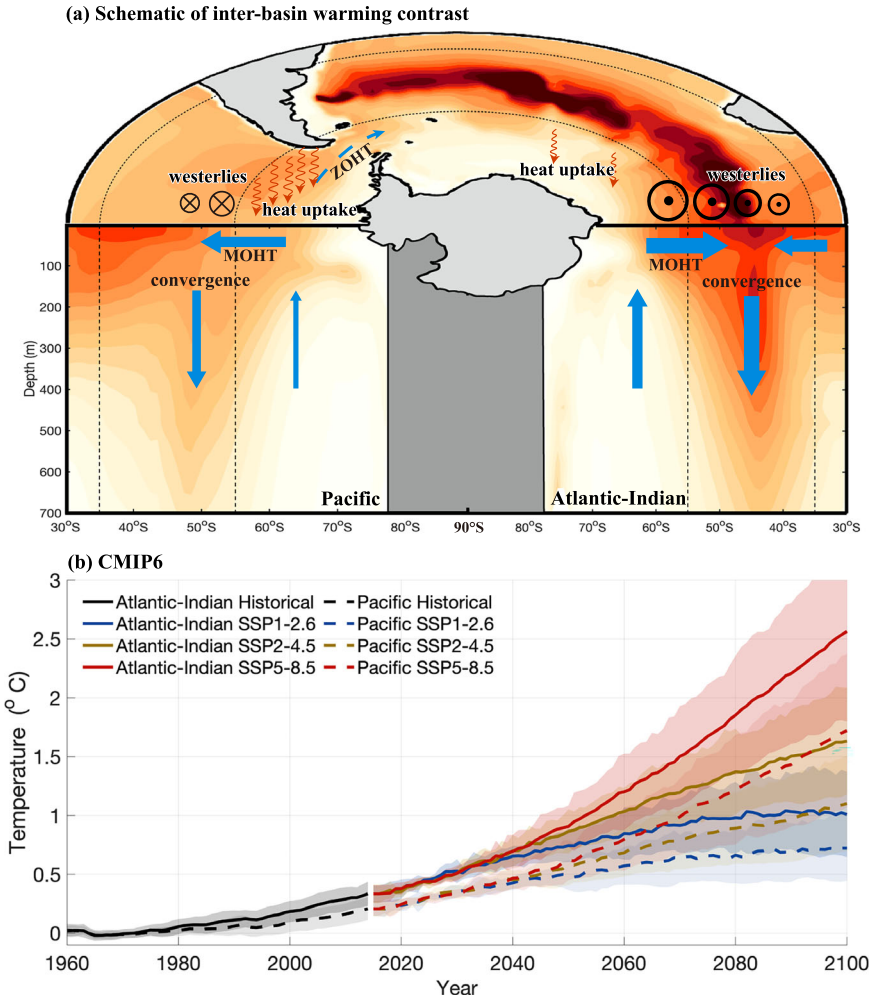

Fig. 6 | Schematic and projection of inter-basin warming contrast in the Southern Ocean. a Schematic of inter-basin warming contrast. Projected temperature change is calculated as the time-mean temperature in 2080-2100 minus that in 1960–1980 from CESM1-LE ensemble mean. Horizontal section shows projected 0–700 m vertical averaged temperature change. Vertical cross-sections demonstrate projected zonal mean temperature change in the Pacific (150°E-70°W) and Atlantic-Indian (70°W-150°E) sectors. **b** Historical simulations (1960–2014) and future projections (2015–2099) of 0–700 m temperature changes of the Pacific and Atlantic-Indian sectors under three Shared Socioeconomic Pathways (SSP1-2.6, SSP2-4.5, and SSP5-8) based on CMIP6 models. Shading denotes the one standard deviation range of model members.

contrast is a robust feature of the SO warming in response to anthropogenic climate change and will persist or amplify in the 21st century. These insights into the inter-basin warming contrast are useful in understanding and predicting regional changes in primary production[60], particularly the key component in the SO food chain—the Antarctic krill[61], which has a large proportion of the population (>50%) in the Atlantic sector[62].

Simulations of ocean models forced with atmospheric reanalysis fields show considerable discrepancies among each other and with observation in detailed features of the SO warming pattern, as suggested by the present (Fig. 5 and Supplementary Fig. 9) and previous studies[30,31]. These discrepancies stem from differences in temporal period, forcing fields, and model physics among these simulations. In addition, the lack of air-sea interaction and uncertainties contained in forcing fields, particularly during pre-satellite era (e.g., prior to 1979), are two major error sources in ocean model simulations. Our LICOM simulations exhibit notable discrepancies from observation. For example, the equatorward shift of the warming band and the overestimated warming near the western boundary of the Pacific sector may result from a warm bias linked to the model's coarse horizontal resolutions and underestimation of mesoscale eddy-induced heat transports. Given these uncertainties, our understanding of the SO's warming structure under greenhouse warming is far from complete. Future work should take advantage of the expanding Argo network to more rigorously assess the robustness of observed and modeled temperature changes. Further efforts are also required to assess the relative contributions of other anthropogenic forcings, such as industrial aerosols, biomass burning aerosols, and ozone. With these regards, we anticipate that more extensive investigations of inter-basin contrast and other asymmetric features of the SO warming in the future, which shall significantly improve our understanding of oceanic storages of anthropogenic heat and carbon.

Methods

Observational datasets

We use three observational ocean datasets for the 1960-2020 period: the Institute of Atmospheric Physics (IAP) ocean analysis data provided by the Chinese Academy of Sciences[7,63], the EN4.2.1 from Met Office Hadley Centre[35,64], and the 2017 version of Ishii data from Meteorological Research Institute, Japan Meteorological Agency[34]. All the three datasets provide monthly fields of analyzed ocean temperature on standard levels with 1° × 1° horizontal resolutions. These datasets are based on all-available historical in-situ ocean temperature data and constructed in different quality control and gap-filling methods. Usage

of the three datasets allows for a comparative analysis. In this study, the linear trend of the 0–700 m ocean heat content (OHC) is computed for the 1960–2020 period, as a quantification of the upper-ocean heat storage. The 0–700 m OHC is calculated as

$$OHC = \int_{-700}^{0} \rho_0 c_p \theta dz \quad (1)$$

where θ is potential temperature, ρ_0 = 1025 kg m^{-3} is the seawater density, and c_p = 3996 JK^{-1}kg^{-1} is the specific heat capacity of seawater. Monthly data of surface heat fluxes and winds of 1960–2020 are primarily derived from ERA5[58], while JRA-55[65,66] is used as a supplementary dataset to examine the robustness of the results. The wind stress curl is calculated as $\frac{\partial \tau_y}{\partial x} - \frac{\partial \tau_x}{\partial y}$, where τ_x and τ_y are zonal and meridional wind stress, respectively. The Ekman transport plays a critical role in northward heat transport in the upper SO[3,19,20], whose vertical component is inversely proportional to the wind stress curl at a fixed latitude.

Climate model simulations

The large ensemble of the Community Earth System Model version 1 (CESM1-LE) provides a 40-member run of coupled simulations with distinct initial conditions and forced by the same radiative forcing scenario[36]. Here we analyze historical run from 1920 to 2005 and a future run under the Representative Concentration Pathway (RCP) 8.5 emission scenario from 2006 to 2100. The ocean component of CESM1 adopts the Parallel Ocean Program (POP) in 1° × 1° resolutions. Here, we analyze monthly data of temperature and ocean horizonal and vertical velocities (including Eulerian mean, mesoscale, and sub-mesoscale processes). The ensemble-mean of CESM1-LE represents externally forced changes by anthropogenic greenhouse gases, aerosols, and ozone, while the spread of model members measures the effect of internal natural variability.

Coupled Model Intercomparison Project phase 6 (CMIP6)[67] provides more comprehensive simulations from various coupled models, under historical forcing of 1850-2014 and three Shared Socioeconomic Pathway (SSP) scenarios (1-2.6, 2-4.5, and 5-8.5) of 2015-2100. The projected results from the multi-model ensemble mean of 13 CMIP6 models (ACCESS-CM2, BCC-CSM2-MR, CAMS-CSM1-0, CESM2-WACCM, CIESM, EC-Earth3, FGOALS, FIO-ESM, GFDL-CM4, MIROC6, MPI-ESM1-2-LR, MRI-ESM2-0, NorESM2-MM) reveals effects of anthropogenic greenhouse warming. We interpolated model outputs to a regular 1° × 1° horizontal grids and analyze annual-mean data of ocean temperature.

Ocean model simulations

Forced ocean models can be utilized to understand specific oceanic responses to global warming-induced changes in surface net heat flux and wind stress via sensitivity experiments. The LASG/IAP Climate Ocean Model (LICOM) version 3[37] is developed by the State Key Laboratory of Numerical Modeling for Atmospheric Sciences and Geophysical Fluid Dynamics (LASG) of the IAP. LICOM features a horizontal resolution of ~1° × 1° and 30 vertical layers extending from the surface to 5500 m. Surface atmospheric forcing is computed from ERA5 using bulk formula, including surface winds, surface shortwave and longwave radiation, near-surface air temperature, specific humidity, precipitation, air density, and sea level pressure. Forced by the repeated daily forcing of 1941–1950, LICOM is spun up for 500 years to reach a quasi-equilibrium state of the ocean. Following the spin-up, the control run (CTRL) is forced by all atmospheric fields from 1940 to 2020 (Lu et al. 2024).

To investigate distinct roles of surface heat flux and surface winds in OHC change, we designed two sensitivity experiments. The heat flux experiment (HTFL) aims to investigate the effect of surface heat uptake, using the same wind stress and precipitation as the spin-up, with other variables matching those in CTRL. The winds experiment (WND) can isolate the role of wind-driven heat redistribution in the SO warming, which uses the same surface wind stress as CTRL, while other variables are kept consistent with the spin-up. Although these idealized experiments are subject to limitations, such as prescribed surface heat flux in WND may inhibit radiative and turbulent feedback associated with SST changes, they enable us to separately examine the impacts of surface heat uptake and wind-driven redistribution on SO warming, providing insights into the mechanisms driving observed changes in this region.

To confirm the simulation of LICOM, we also performed a simulation with the Massachusetts Institute of Technology General Circulation Model (MITgcm)[59] Ocean Comprehensible Atlas 2 (OCCA2)[68] also forced with ERA5 reanalysis from 1960 to 2024. The simulation is based on the same model configuration as Estimating the Circulation and Climate of the Ocean Version 4 (ECCO4) release 2[69] with a nominal horizontal resolution of 1 degree. The only differences compared with ECCO4 release 2 are the initial conditions and forcing fields. Atmosphere forcing was replaced with ERA5 plus climatological monthly mean adjustment, which was calculated to match ECCO4 release 2 forcing over 1992-2011. Initial conditions from 1992 were used to carry out a ten-year spin-up from 1960 to 1970. The result for January 1st 1970 was then used to initialize the OCCA2 simulation which starts January 1st 1960.

Heat transports

The meridional ocean heat transport (MOHT) in the 0–100 m layer (almost the Ekman layer) is calculated as

$$MOHT = \int_{-100}^{0} \int_{x1}^{x2} \rho_0 c_p v\theta \, dxdz \quad (2)$$

where v is the "residual" meridional velocity[2,70] in CESM1-LE, including contributions from Eulerian mean circulation, mesoscale eddies, and sub-mesoscale processes. The meridional gradient of MOHT, $\partial MOHT/\partial y$, represents divergent cooling (positive) and convergent heating (negative) induced by MOHT. The estimated Ekman MOHT based on τ_x in ERA5 and temperature in IAP is calculated as

$$MOHT_E = \int_{-100}^{0} \int_{x1}^{x2} \rho_0 c_p \left(-[\theta] \frac{\tau_x}{f \rho_0} \right) dx \quad (3)$$

where $[\theta]$ is the vertical mean temperature of 0–100 m. The vertical heat flux is computed as $\rho_0 c_p w\theta$, where w is the residual vertical velocity in CESM1-LE. All zonal mean figures in this paper are divided by corresponding zonal distance (m^{-1}) to properly compare property differences in the Atlantic-Indian and Pacific sectors. Zonal ocean heat transport (ZOHT) at a given longitude is calculated as

$$ZOHT = \int_{-700}^{0} \int_{y1}^{y2} \rho_0 c_p u\theta \, dydz \quad (4)$$

where u is the residual zonal velocity in CESM-LE. We calculate the ZOHT of the 0-700 m, 90°S-35°S sections at 150°E and 70°W, to represent the heat transport into and out of the Pacific sector, respectively.

Data availability

The minimum dataset required to interpret, verify, and extend the results of this article is available from (https://doi.org/10.5281/zenodo.16116786). The observational and reanalysis data used in this study are publicly available. IAP data are available at (http://www.ocean.iap.ac.cn). EN4.2.1 data are available at (https://www.metoffice.gov.uk/hadobs/en4/). Ishii data are available at (https://www.data.jma.go.jp/

kaiyou/english/ohc/ohc_data_en.html). ERA5 reanalysis data were obtained from the ECMWF data server (https://www.ecmwf.int/en/forecasts/dataset/ecmwf-reanalysis-v5). CESM1-LE simulations can be found at (https://www.cesm.ucar.edu/community-projects/lens/data-sets). LICOM and MITgcm outputs are available upon request. CMIP6 simulations can be obtained from (https://esgf-node.ipsl.upmc.fr/projects/cmip6-ipsl/).

Code availability

The LICOM source code is available at (https://github.com/yongqiangyu/FGOALS.git); The data generated in this study have been deposited in the Zenodo database under accession MATLAB code: (https://doi.org/10.5281/zenodo.16116786).

References

1. Williams, R. G. et al. Asymmetries in the Southern Ocean contribution to global heat and carbon uptake. *Nat. Clim. Change* https://doi.org/10.1038/s41558-024-02066-3 (2024).
2. Liu, W., Lu, J., Xie, S.-P. & Fedorov, A. Southern Ocean heat uptake, redistribution, and storage in a warming climate: the role of meridional overturning circulation. *J. Clim.* **31**, 4727–4743 (2018).
3. Swart, N. C., Gille, S. T., Fyfe, J. C. & Gillett, N. P. Recent Southern Ocean warming and freshening driven by greenhouse gas emissions and ozone depletion. *Nat. Geosci.* **11**, 836–841 (2018).
4. Gille, S. T. Warming of the Southern Ocean Since the 1950s. *Science* **295**, 1275–1277 (2002).
5. Böning, C. W., Dispert, A., Visbeck, M., Rintoul, S. R. & Schwarzkopf, F. U. The response of the Antarctic circumpolar current to recent climate change. *Nat. Geosci.* **1**, 864–869 (2008).
6. Shi, J.-R., Xie, S.-P. & Talley, L. D. Evolving Relative Importance of the Southern Ocean and North Atlantic in Anthropogenic Ocean heat uptake. *J. Clim.* **31**, 7459–7479 (2018).
7. Cheng, L. et al. Improved estimates of ocean heat content from 1960 to 2015. *Sci. Adv.* **3**, e1601545 (2017).
8. Sallée, J.-B. Southern Ocean warming. *Oceanography* **31**, 52–62 (2018).
9. Cheng, L. et al. Past and future ocean warming. *Nat. Rev. Earth Environ.* **3**, 776–794 (2022).
10. Purich, A. & Doddridge, E. W. Record low Antarctic sea ice coverage indicates a new sea ice state. *Commun. Earth Environ.* **4**, 314 (2023).
11. Paolo, F. S., Fricker, H. A. & Padman, L. Volume loss from Antarctic ice shelves is accelerating. *Science* **348**, 327–331 (2015).
12. Purkey, S. G. & Johnson, G. C. Warming of global abyssal and deep Southern Ocean waters between the 1990s and 2000s: contributions to global heat and sea level rise budgets. *J. Clim.* **23**, 6336–6351 (2010).
13. Shimada, K., Aoki, S., Ohshima, K. I. & Rintoul, S. R. Influence of Ross Sea Bottom water changes on the warming and freshening of the Antarctic Bottom Water in the Australian-Antarctic Basin. *Ocean Sci.* **8**, 419–432 (2012).
14. Gunn, K. L., Rintoul, S. R., England, M. H. & Bowen, M. M. Recent reduced abyssal overturning and ventilation in the Australian Antarctic Basin. *Nat. Clim. Change* **13**, 537–544 (2023).
15. Venegas, R. M., Acevedo, J. & Treml, E. A. Three decades of ocean warming impacts on marine ecosystems: A review and perspective. *Deep Sea Res. Part II Top. Stud. Oceanogr.* **212**, 105318 (2023).
16. Liu, W., Li, S., Li, C., Rugenstein, M. & Thomas, A. P. Contrasting fast and slow intertropical convergence zone migrations linked to delayed Southern Ocean warming. *Nat. Clim. Change* https://doi.org/10.1038/s41558-024-02034-x (2024).
17. Wang, G. et al. Future Southern Ocean warming linked to projected ENSO variability. *Nat. Clim. Change* **12**, 649–654 (2022).
18. Cai, W., Cowan, T., Godfrey, S. & Wijffels, S. Simulations of processes associated with the fast warming rate of the Southern Midlatitude Ocean. *J. Clim.* **23**, 197–206 (2010).
19. Armour, K. C., Marshall, J., Scott, J. R., Donohoe, A. & Newsom, E. R. Southern Ocean warming delayed by circumpolar upwelling and equatorward transport. *Nat. Geosci.* **9**, 549–554 (2016).
20. Cai, W. et al. Southern Ocean warming and its climatic impacts. *Sci. Bull.* **68**, 946–960 (2023).
21. Morrison, A. K., Griffies, S. M., Winton, M., Anderson, W. G. & Sarmiento, J. L. Mechanisms of Southern Ocean heat uptake and transport in a global eddying climate model. *J. Clim.* **29**, 2059–2075 (2016).
22. Marshall, J. & Speer, K. Closure of the meridional overturning circulation through Southern Ocean upwelling. *Nat. Geosci.* **5**, 171–180 (2012).
23. Llovel, W. & Terray, L. Observed southern upper-ocean warming over 2005–2014 and associated mechanisms. *Environ. Res. Lett.* **11**, 124023 (2016).
24. Abernathey, R. P. et al. Water-mass transformation by sea ice in the upper branch of the Southern Ocean overturning. *Nat. Geosci.* **9**, 596–601 (2016).
25. Gao, L., Rintoul, S. R. & Yu, W. Recent wind-driven change in Subantarctic mode water and its impact on ocean heat storage. *Nat. Clim. Change* **8**, 58–63 (2018).
26. Liu, L., Li, Y., Wang, F. & Ren, Q. Heat transport into the interior ocean induced by water-mass subduction. *Environ. Res. Lett.* **19**, 074002 (2024).
27. Fyfe, J. C., Saenko, O. A., Zickfeld, K., Eby, M. & Weaver, A. J. The role of poleward-intensifying winds on Southern Ocean warming. *J. Clim.* **20**, 5391–5400 (2007).
28. Karsten, R. H. & Marshall, J. Constructing the residual circulation of the ACC from Observations. *J. Phys. Oceanogr.* **32**, 3315–3327 (2002).
29. Zhang, Z. et al. Submesoscale inverse energy cascade enhances Southern Ocean eddy heat transport. *Nat. Commun.* **14**, 1335 (2023).
30. Huguenin, M. F., Holmes, R. M. & England, M. H. Drivers and distribution of global ocean heat uptake over the last half century. *Nat. Commun.* **13**, 4921 (2022).
31. Hague, M., Münnich, M. & Gruber, N. Zonally Asymmetric Increase in Southern Ocean heat content. *J. Clim.* https://doi.org/10.1175/JCLI-D-23-0623.1 (2024).
32. Song, Y. et al. Decadal thermal variability of the upper Southern Ocean: zonal asymmetry. *J. Clim.* **37**, 3117–3132 (2024).
33. Cheng, L. & Zhu, J. Benefits of CMIP5 multimodel ensemble in reconstructing historical ocean subsurface temperature variations. *J. Clim.* **29**, 5393–5416 (2016).
34. Ishii, M. et al. Accuracy of global upper ocean heat content estimation expected from present observational data sets. *Sola* **13**, 163–167 (2017).
35. Good, S. A., Martin, M. J. & Rayner, N. A. EN4: quality controlled ocean temperature and salinity profiles and monthly objective analyses with uncertainty estimates. *J. Geophys. Res. Oceans* **118**, 6704–6716 (2013).
36. Kay, J. E. et al. The community earth system model (CESM) large ensemble project: a community resource for studying climate change in the presence of internal climate variability. *Bull. Am. Meteorol. Soc.* **96**, 1333–1349 (2015).
37. Lin, P. et al. LICOM model datasets for the CMIP6 ocean model intercomparison project. *Adv. Atmos. Sci.* **37**, 239–249 (2020).
38. Sallée, J.-B. et al. Assessment of Southern Ocean mixed-layer depths in CMIP5 models: Historical bias and forcing response. *J. Geophys. Res. Oceans* **118**, 1845–1862 (2013).
39. Hyder, P. et al. Critical Southern Ocean climate model biases traced to atmospheric model cloud errors. *Nat. Commun.* **9**, 3625 (2018).
40. Garuba, O. A. & Klinger, B. A. Ocean heat uptake and interbasin transport of the passive and redistributive components of surface heating. *J. Clim.* **29**, 7507–7527 (2016).

41. Banks, H. T. & Gregory, J. M. Mechanisms of ocean heat uptake in a coupled climate model and the implications for tracer based predictions of ocean heat uptake. *Geophys. Res. Lett.* **33**, L07608 (2006).
42. Shi, J.-R., Talley, L. D., Xie, S.-P., Liu, W. & Gille, S. T. Effects of Buoyancy and Wind Forcing on Southern Ocean Climate Change. *J. Clim.* **33**, 10003–10020 (2020).
43. Lyu, K. et al. Roles of Surface Forcing in the Southern Ocean temperature and salinity changes under Increasing CO_2: perspectives from model perturbation experiments and a theoretical framework. *J. Phys. Oceanogr.* **53**, 19–36 (2023).
44. Waugh, D. W., Primeau, F., DeVries, T. & Holzer, M. Recent changes in the ventilation of the Southern Oceans. *Science* **339**, 568–570 (2013).
45. Cai, W. & Cowan, T. Trends in Southern Hemisphere circulation in IPCC AR4 Models over 1950–99: ozone depletion versus greenhouse forcing. *J. Clim.* **20**, 681–693 (2007).
46. Lee, S. & Feldstein, S. B. Detecting ozone- and greenhouse gas–driven wind trends with observational data. *Science* **339**, 563–567 (2013).
47. Ding, Q., Steig, E. J., Battisti, D. S. & Küttel, M. Winter warming in West Antarctica caused by central tropical Pacific warming. *Nat. Geosci.* **4**, 398–403 (2011).
48. Li, X. et al. Tropical teleconnection impacts on Antarctic climate changes. *Nat. Rev. Earth Environ.* **2**, 680–698 (2021).
49. Duan, J. et al. Rapid Sea Level Rise in the Southern Hemisphere Subtropical Oceans. *J. Clim.* **34**, 9401–9423 (2021).
50. Zhang, L., Delworth, T. L., Cooke, W. & Yang, X. Natural variability of Southern Ocean convection as a driver of observed climate trends. *Nat. Clim. Change* **9**, 59–65 (2019).
51. Yin, J. H. A consistent poleward shift of the storm tracks in simulations of 21st century climate. *Geophys. Res. Lett.* **32**, L18701 (2005).
52. Swart, N. C. & Fyfe, J. C. Observed and simulated changes in the Southern Hemisphere surface westerly wind-stress. *Geophys. Res. Lett.* **39**, L16711 (2012).
53. Collins, M. et al. In *Climate Change 2013 – The Physical Science Basis: Working Group I Contribution to the Fifth Assessment Report of the Intergovernmental Panel on Climate Change* (Cambridge University Press, Cambridge, 2013).
54. Goyal, R., Sen Gupta, A., Jucker, M. & England, M. H. Historical and Projected Changes in the Southern Hemisphere Surface Westerlies. *Geophys. Res. Lett.* **48**, e2020GL090849 (2021).
55. Russell, J. L., Dixon, K. W., Gnanadesikan, A., Stouffer, R. J. & Toggweiler, J. R. The Southern Hemisphere Westerlies in a warming world: propping open the door to the Deep Ocean. *J. Clim.* **19**, 6382–6390 (2006).
56. O'Connor, G. K., Steig, E. J. & Hakim, G. J. Strengthening Southern Hemisphere Westerlies and Amundsen Sea low deepening over the 20th century revealed by proxy-data assimilation. *Geophys. Res. Lett.* **48**, e2021GL095999 (2021).
57. Shi, J.-R., Talley, L. D., Xie, S.-P., Peng, Q. & Liu, W. Ocean warming and accelerating Southern Ocean zonal flow. *Nat. Clim. Change* **11**, 1090–1097 (2021).
58. Hersbach, H. et al. The ERA5 global reanalysis. *Q. J. R. Meteorol. Soc.* **146**, 1999–2049 (2020).
59. Marshall, J., Adcroft, A., Hill, C., Perelman, L. & Heisey, C. A finite-volume, incompressible Navier Stokes model for studies of the ocean on parallel computers. *J. Geophys. Res. Oceans* **102**, 5753–5766 (1997).
60. Constable, A. J., Nicol, S. & Strutton, P. G. Southern Ocean productivity in relation to spatial and temporal variation in the physical environment. *J. Geophys. Res. Oceans* **108**, 8079 (2003).
61. Kawaguchi, S. et al. Climate change impacts on Antarctic krill behaviour and population dynamics. *Nat. Rev. Earth Environ.* **5**, 43–58 (2024).
62. Murphy, E. J. et al. Restricted regions of enhanced growth of Antarctic krill in the circumpolar Southern Ocean. *Sci. Rep.* **7**, 6963 (2017).
63. Cheng, L., Trenberth, K. E., Palmer, M. D., Zhu, J. & Abraham, J. P. Observed and simulated full-depth ocean heat-content changes for 1970–2005. *Ocean Sci.* **12**, 925–935 (2016).
64. Gouretski, V. & Reseghetti, F. On depth and temperature biases in bathythermograph data: Development of a new correction scheme based on analysis of a global ocean database. *Deep Sea Res. Part Oceanogr. Res. Pap.* **57**, 812–833 (2010).
65. Kobayashi, S. et al. The JRA-55 reanalysis: general specifications and basic characteristics. *J. Meteorol. Soc. Jpn. Ser. II* **93**, 5–48 (2015).
66. Harada, Y. et al. The JRA-55 reanalysis: representation of atmospheric circulation and climate variability. *J. Meteorol. Soc. Jpn. Ser. II* **94**, 269–302 (2016).
67. Eyring, V. et al. Overview of the Coupled Model Intercomparison Project Phase 6 (CMIP6) experimental design and organization. *Geosci. Model Dev.* **9**, 1937–1958 (2016).
68. Forget, G. Mapping Ocean observations in a dynamical framework: a 2004–06 Ocean Atlas. *J. Phys. Oceanogr.* **40**, 1201–1221 (2010).
69. Forget, G. et al. ECCO version 4: an integrated framework for non-linear inverse modeling and global ocean state estimation. *Geosci. Model Dev.* **8**, 3071–3104 (2015).
70. Marshall, J. & Radko, T. Residual-mean solutions for the antarctic circumpolar current and its associated overturning circulation. *J. Phys. Oceanogr.* **33**, 2341–2354 (2003).

Acknowledgements

This study was supported by the National Natural Science Foundation of China (42406024), the Laoshan Laboratory (LSKJ202202601), and the Oceanographic Data Center, Institute of Oceanology, Chinese Academy of Sciences for Y.L. G.F. was supported by NASA awards 80NSSC20K0796, 80NSSC23K0355 (also support Y.S.), 80NSSC22K1697, 1676067, and 1686358, as well as from the Simons Foundation via the CBIOMES and SCOPE-GRADIENTS program is acknowledged for this work. Q.L. is supported by the NASA MAP program 19-MAP19-0011 and the MIT-GISS cooperative agreement. This work is also partially supported by the Regional and Global Model Analysis (RGMA) component of the Earth and Environmental System Modeling Program of the U.S. Department of Energy's Office of Biological & Environmental Research (BER) via National Science Foundation (NSF) IA 1947282 (DE-SC0022070) for A.H. The National Center for Atmospheric Research is sponsored by the NSF of the United States of America under Cooperative Agreement No. 1852977.

Author contributions

Y.S. and Y.L. conceived this study. Y.S. wrote the initial manuscript and performed the analyses in discussion with Y.L., G.F., A.H., Q.L., J.S., X.C. and F.W. K.G. carried out LICOM experiments. G.F. carried out MITgcm experiments. All authors contributed to interpreting results, discussion, and improvement of this paper.

Competing interests

The authors declare no competing interests.

Additional information

Supplementary information The online version contains supplementary material available at (https://doi.org/10.1038/s41467-025-64112-8).

Correspondence and requests for materials should be addressed to Yuanlong Li.

Peer review information *Nature Communications* thanks the anonymous, reviewer(s) for their contribution to the peer review of this work. A peer review file is available.